Journal of Computational Physics **170,** 184–204 (2001)
doi:10.1006/jcph.2001.6732, available online at http://www.idealibrary.com on IDEAL®

# A Class of Explicit ENO Filters with Application to Unsteady Flows

Eric Garnier,* Pierre Sagaut,*[,1] and Michel Deville†

*ONERA, 29, Avenue de la Division Leclerc, BP72 92322 Châtillon Cedex, France; and †Laboratoire de Mécanique des Fluides, Ecole Polytechnique Fédérale de Lausanne, CH-1015 Lausanne, Switzerland
E-mail: egarnier@onera.fr, sagaut@onera.fr, michel.deville@epfl.ch

Received February 8, 2000; revised August 29, 2000

ENO filters are developed and compared with classical ENO schemes, TVD filters, and classical TVD schemes. The amplitude of the numerical dissipation provided by the filtering pass is computed by means of the artificial compression method (ACM) switch and it is demonstrated that the use of this sensor improves markedly the quality of results compared to classical approaches (shock-capturing schemes) in laminar unsteady flows. On a fully turbulent flow, it is demonstrated that the ACM sensor is not able to distinguish a turbulent fluctuation from a shock, whereas the sensor proposed by Ducros *et al*. [9] makes easily this distinction. © 2001 Academic Press

*Key Words:* shock-capturing schemes; filters; sensors; large-eddy simulation.

## 1. INTRODUCTION

The main difficulty in the application of large-eddy simulation (LES) to compressible flows is the control of the numerical dissipation necessary to capture discontinuities that can occur in such flows. In a previous study [1], in the framework of freely decaying turbulence, it was shown that the numerical dissipation of high-order accurate, shock-capturing schemes masks the effect of the subgrid-scale (SGS) models. In another study, Lee *et al*. [2] have noticed that the use of a sixth-order accurate, essentially nonoscillatory (ENO) scheme in the entire computational domain leads to a significant damping of the turbulent fluctuations. A local application of the shock-capturing scheme is then absolutely necessary to minimize the numerical dissipation. In the study of Lee *et al*. [2], this requirement is achieved by means of the application of the ENO scheme only in the shock-normal direction and over a few mesh points around the mean shock position which is known in that particular case of shock/homogeneous turbulence interaction. This approach leads to very satisfying results in

[1] To whom correspondence should be addressed.



0021-9991/01 $35.00

this configuration for direct numerical simulation (DNS) [2] and for large-eddy simulation [3, 4]. Unfortunately, in most cases, the shock position is unknown, and one needs to introduce a sensor to detect possible discontinuities.

Concerning the computations of flows with shocks, methods designed to regularize a numerical solution are studied since the early attempts of von Neumann and Richtmyer [5] who used finite difference technique combined with the so-called artificial viscosity. Later, Engquist *et al*. [6] have derived a set of explicit nonlinear filters which improve the computational efficiency with respect to the previous approach. This method can be easily implemented into existing codes because the filter step is essentially independent of the basic differencing scheme and is presented as a postprocessing. The advantage compared to classical shock-capturing schemes, is the low cost of this method since the filtering pass is applied once per time step while a shock-capturing scheme is applied at each substep of a time advancement procedure. In the same way, Yee *et al*. [7] show that the dissipative part of a shock-capturing scheme can be applied after each time step to regularize the solution and acts like a filter. Moreover, to meet the requirement of a local application of the numerical dissipation, they demonstrate that the amplitude of the dissipation can be evaluated with a sensor derived from the artificial compression method (ACM) of Harten [8]. Unfortunately, the ability of the sensor was not demonstrated on a fully turbulent case. Another point of minor importance is the parameter dependence on the amplitude of the introduced numerical dissipation.

The numerical tests provided in [7] are restricted to total variation diminishing (TVD) schemes. The possibility of using ENO schemes is mentioned but the developments are not provided. In this paper, we derived a class of high-order, nonlinear filters based on ENO reconstruction, and numerical tests are carried out to evaluate their accuracy with respect to TVD filters. Furthermore, to improve the Jameson sensor which was found unable to distinguish a shock from a turbulent fluctuation, Ducros *et al*. [9] have derived a new sensor. In this study, both ACM and Ducros *et al*. [9] sensors are compared on fully turbulent test cases.

The paper is organized as follows. First, the Yee *et al*. [7] approach is recalled, its extension to ENO schemes is introduced, and the sensor of Ducros *et al*. [9] is presented. In Section 3, ENO filters are compared to classical ENO schemes and to TVD filters in academic test cases such as the transport of an isotropic vortex, the interaction of a density wave with a shock, and the shock/vortex interaction. In Section 4, ACM and Ducros *et al*. [9] sensors are compared to two three-dimensional cases: freely decaying homogeneous turbulence and shock/homogeneous turbulence interaction. The general conclusion is presented in Section 5.

## 2. CHARACTERISTIC BASED FILTERS

### 2.1. *Governing Equations*

Governing equations are the unsteady dimensionless compressible Navier–Stokes equations written in Cartesian coordinates, expressed in 2D for sake of brevity

$$\frac{\partial U}{\partial t} + \frac{\partial F}{\partial x} + \frac{\partial G}{\partial y} + \frac{\partial F_v}{\partial x} + \frac{\partial G_v}{\partial y} = 0, \tag{1}$$

where $t$ is the dimensionless time and $x$ and $y$ represent respectively the streamwise and the vertical directions. The solution vector $U$ is based on the conservative variables, $F$ and $G$ are the convective fluxes, and $F_v$ and $G_v$ denote the viscous fluxes

$$U = \begin{bmatrix} \rho \\ \rho u \\ \rho v \\ \rho E \end{bmatrix}; \quad F = \begin{bmatrix} \rho u \\ \rho u^2 + P \\ \rho uv \\ \rho uE + uP \end{bmatrix}; \quad G = \begin{bmatrix} \rho v \\ \rho uv \\ \rho v^2 + P \\ \rho vE + vP \end{bmatrix}$$

$$F_v = \begin{bmatrix} 0 \\ \sigma_{11} \\ \sigma_{12} \\ u\sigma_{11} + v\sigma_{12} + \Phi_1 \end{bmatrix}; \quad G_v = \begin{bmatrix} 0 \\ \sigma_{12} \\ \sigma_{22} \\ u\sigma_{12} + v\sigma_{22} + \Phi_2 \end{bmatrix},$$

where $\rho$ is the density, $u$, $v$ are the $x$ and $y$ velocity components, and $E$ is the total energy per unit mass. The stress tensor and the heat flux components are then expressed as

$$\sigma_{ij} = -2\frac{\mu}{\mathrm{Re}_0}\left(S_{ij} - \frac{1}{3}S_{kk}\delta_{ij}\right) \tag{2}$$

$$\Phi_i = \frac{-\mu}{(\gamma - 1)\,\mathrm{Re}_0 \mathrm{Pr}_0 M_0^2}\frac{\partial T}{\partial x_i}, \tag{3}$$

where $S_{ij}$ is the strain rate tensor:

$$S_{ij} = \frac{1}{2}\left(\frac{\partial u_i}{\partial x_j} + \frac{\partial u_j}{\partial x_i}\right).$$

As usual, $T$ and $P$ denote respectively the temperature and the pressure. They are related to the conservative variables by using an equation of state written for a perfect gas

$$P = (\gamma - 1)\left[\rho E - \frac{1}{2}\frac{(\rho u)^2 + (\rho v)^2}{\rho}\right] \tag{4}$$

$$T = \gamma M_0^2 \frac{P}{\rho}. \tag{5}$$

For sake of simplicity, the study is restricted to ideal gas with constant specific heat ratio ($\gamma = 1.4$), constant viscosity coefficient ($\mu = \mu(T_0)$), and constant Prandtl number ($\mathrm{Pr}_0 = 0.7$). The Reynolds number ($\mathrm{Re}_0$) is based on the reference values of the density ($\rho_0$), velocity ($V_0$), and length–scale ($L_0$). The Mach number is defined as $M_0 = V_0/(\gamma R T_0)$ ($R$ is the gas constant and $T_0$ is the reference temperature).

### 2.2. *High-Order Nonlinear Filters*

If $U^n$ denotes the vector of the conservative variables evaluated at the time $n\Delta t$ and $\Delta t$ is the time step, $\hat{U}^{(n+1)}$ is the vector of the conservative variables after the application of any explicit time advancement scheme. This vector is spatially filtered to give the final state

$U^{n+1}$ ($U^{n+1} = \mathcal{F}(\hat{U}^{(n+1)})$). The main point is that the time advancement is conducted with a nondissipative spatial operator (noted $L$). The filtering pass is decomposed as

$$U^{(n+1)} = \mathcal{F}\left(\hat{U}^{(n+1)}\right) = (I_d + \Delta t L_f)\left(\hat{U}^{(n+1)}\right), \tag{6}$$

where $L_f$ is any dissipative operator and $I_d$ is the identity.

In this study, the time integration is performed by means of a third-order accurate TVD Runge-Kutta method proposed by Shu and Osher [10]:

$$\begin{aligned} U^{(1)} &= U^n + \Delta t L(U^n) \\ U^{(2)} &= \frac{3}{4}U^n + \frac{1}{4}U^{(1)} + \frac{1}{4}\Delta t L\left(U^{(1)}\right) \\ \hat{U}^{(n+1)} &= \frac{1}{3}U^n + \frac{2}{3}U^{(2)} + \frac{2}{3}\Delta t L\left(U^{(2)}\right). \end{aligned} \tag{7}$$

Note that $L$ is referred to as "base scheme" and can be any $q$th-order accurate, finite volume or finite difference nondissipative scheme.

As mentioned by Yee *et al*. [7], $L_f$ can be the dissipative part of any shock-capturing scheme and can be expressed as

$$L_f\left(\hat{U}^{(n+1)}\right) = L_f(F^*, G^*) = \frac{1}{\Delta x}\left[F^*_{i+1/2,j} - F^*_{i-1/2,j}\right] + \frac{1}{\Delta y}\left[G^*_{i,j+1/2} - G^*_{i,j-1/2}\right], \tag{8}$$

where $F^*_{i+1/2,j}$ and $G^*_{i,j+1/2}$ are the dissipative numerical fluxes for the filter operator. For a TVD–MUSCL scheme, $L_{\text{muscl}}$ can be written [7]

$$F^{\text{muscl}}_{i+1/2,j} = \frac{1}{2}R_{i+1/2}\Phi_{i+1/2}. \tag{9}$$

The element of $\Phi_{i+1/2}$ denoted $\phi^l_{i+1/2}$ and the vector $\alpha_{i+1/2}$ are given by

$$\phi^l_{i+1/2} = \kappa\theta^l_{i+1/2}\left|a^l_{i+1/2}\right|\alpha^l_{i+1/2} \tag{10}$$

$$\alpha^l_{i+1/2} = R^{-1}_{i+1/2}\left(U^R_{i+1/2} - U^L_{i+1/2}\right), \tag{11}$$

where $a^l_{i+1/2}$ ($\mathrm{l} = 1, \ldots, 4$) are the eigenvalues and $R_{i+1/2}$ is the eigenvector matrix of $\frac{\partial F}{\partial U}$ evaluated using a symmetric average between $U^R_{i+1/2}$ and $U^L_{i+1/2}$, which are the upwind-biased interpolation of the neighboring $U_j$ values with the slope limiters imposed (see [11] for details).

The amplitude of the dissipation applied to each characteristic wave is evaluated with the discontinuity sensor $\theta^l_{i+1/2}$. The sensor chosen in [7] is the Harten switch [8] originally designed for self-adjusting hybrid schemes between Harten's first-order, ACM scheme and higher order schemes.

Following the simplifications recommended by Yee *et al.* [7], the Harten's switch is expressed as

$$\theta^l_{i+1/2} = \max\left(\theta^l_i, \theta^l_{i+1}\right), \tag{12}$$

with

$$\theta_i^l = \left| \frac{|\alpha_{i+1/2}^l| - |\alpha_{i-1/2}^l|}{|\alpha_{i+1/2}^l| + |\alpha_{i-1/2}^l|} \right|. \tag{13}$$

The constant $\kappa$ is problem dependent and may vary in the range $0.03 < \kappa < 2$. Moreover, $\kappa$ can take different values for each characteristic wave. For a mixing layer test case including shocks, Yee *et al.* [7] have used $\kappa = 0.7$ for nonlinear waves and $\kappa = 0.35$ for linear waves. Here, this case-to-case adaptation is avoided and the value of $\kappa$ is fixed to 1. Note that, with such a value of $\kappa$, the numerical dissipation introduced by $L_{\text{muscl}}$ cannot be larger than the dissipation introduced by a MUSCL scheme without any sensor, since $\theta^l$ varies in the range $[0, 1]$.

This approach can be extended to $r$th-order accurate, ENO schemes. The dissipative part of the ENO scheme is obtained by subtracting a $m$th-order accurate, centered scheme to an $r$th-order accurate, ENO scheme.

$$F_{i+1/2,j}^{\text{eno}} = R_{i+1/2} \Phi_{i+1/2}, \tag{14}$$

with

$$\phi_{i+1/2}^l = \theta_{i+1/2}^l \left( \sum_{p=0}^{r-1} \vartheta_{k,p}^r R_{i+1/2}^{-1} F_{i-r+1+k+p} - \sum_{p=0}^{m-1} \vartheta_{m/2,p}^m R_{i+1/2}^{-1} F_{i-m+1+m/2+p} \right), \tag{15}$$

where $\vartheta_{k,p}^r$ are the reconstruction coefficients (given in [12]) of the ENO procedure, and $k$ is the stencil index selected among the $r$ candidate stencils. This stencil, called $S_k$, is defined as

$$S_k = (x_{i+k-r+1}, x_{i+k-r+2}, \ldots, x_{i+k}), \quad k = 0, \ldots, r-1. \tag{16}$$

Note that the $m$th-order accurate, centered scheme is a particular subclass of ENO scheme with the stencil index $k$ of the reconstruction coefficient $\vartheta_{k,p}^m$ set to $m/2$. Obviously, the order of the centered scheme $m$ is even. Whatever the value of $m \geq 2$, this method allows us to exhibit the dissipative terms of the truncation errors. Nonetheless, in order to keep the precision of the base scheme, it is necessary to chose $m = q$. A larger value of $m$ does not improve the formal global precision.

To increase the order of accuracy with respect to ENO filters, WENO filters can be derived:

$$\phi_{i+1/2}^l = \sum_{k=0}^{r-1} \omega_k \left[ \theta_{i+1/2}^l \left( \sum_{p=0}^{r-1} \vartheta_{k,p}^r R_{i+1/2}^{-1} F_{i-r+1+k+p} - \sum_{p=0}^{m-1} \vartheta_{m/2,p}^m R_{i+1/2}^{-1} F_{i-m+1+m/2+p} \right) \right]. \tag{17}$$

The WENO approach consists of performing linear combinations of the $r$ possible $r$th-order ENO fluxes. The weights $\omega_k$ adapt themselves to the relative smoothness of the flow on each candidate stencil in such a way that the stencils which contain a discontinuity are assigned a nearly zero weight. In absence of discontinuity the choice of optimal weights allow us to increase the order of accuracy of the WENO schemes up to $(2r-1)$th-order of

accuracy. The procedure used to compute the $\omega_k$ is described by Jiang and Shu [12]. The ENO schemes are combined with a Roe solver for all the results presented here.

Another recent procedure to apply the numerical dissipation locally is described in Ducros *et al.* [9]. These authors have remarked that the Jameson sensor [13] takes large values not only in presence of shock but also in presence of turbulent fluctuations. In order to adapt the Jameson scheme to LES, these authors suggest multiplying the Jameson sensor (which fixes the amplitude of the second-order dissipation) by another sensor

$$\Psi = \frac{(\mathrm{div}(\mathbf{u}))^2}{(\mathrm{div}(\mathbf{u}))^2 + (\mathrm{rot}(\mathbf{u}))^2}, \tag{18}$$

where $\mathbf{u}$ denotes the velocity vector. This sensor takes low values where the flow is turbulent (without any shock) and values close to 1 in presence of a shock.

This sensor can be included in our formalism by recasting Eq. (6) as

$$U^{(n+1)} = (Id + \Psi \Delta t L_f)\left(\hat{U}^{(n+1)}\right). \tag{19}$$

The corresponding schemes are referred to as $\Psi$-(name of the scheme)-ACM. Note that it is also possible to approach the formalism described in [9] using the $\Psi$ sensor without the ACM one ($\theta_i^l = 1$). The corresponding schemes are referred to as $\Psi$-(name of the scheme).

## 3. ASSESSMENT OF ENO AND WENO FILTERS

The ENO and WENO filters are compared to TVD–MUSCL filters on three academic cases: the advection of an isentropic vortex [14, 15], the interaction of a moving shock with a density wave [10] at $Ma = 3$, and the shock/vortex interaction (described in [16]). The Ducros *et al.* [9] sensor is not tested here since its use is particularly interesting for fully turbulent flows. For all the computations presented here, the base scheme is a fourth-order accurate, conservative centered scheme [17]. This scheme, used alone, is referred to as C4 and compared with a third-order accurate, ENO scheme [10], a third-order accurate, MUSCL scheme [11], a fifth-order accurate, WENO scheme [12], and their counterparts as characteristic-based filters referred to as, respectively, ENO–ACM, MUSCL–ACM, and WENO–ACM. The formal order of accuracy of ENO–ACM and MUSCL–ACM is limited to 3, whereas the order WENO–ACM is supposed to be the same as the C4 scheme. The MUSCL scheme is used with a minmod limiter function given in [11]. The compression factor in the minmod function is set to 4 to limit the numerical dissipation of the MUSCL scheme. The ENO scheme is implemented here with the modification proposed by Shu [18] who suggests to bias the selection of the stencil toward the most centered one in smooth regions of the flow.

### 3.1. *Advection of an Isentropic Vortex*

To measure the order of accuracy of the characteristic-based filters in a realistic flow, the advection of an isentropic vortex in a free stream is simulated. This case is of particular interest since the solution at any time $t > t_0$ is the initial solution translated over a distance $u_\infty(t - t_0)$. This allows a reliable measure of the order of accuracy.

The mean flow is $\rho_\infty = 1$, $P_\infty = 1$, $T_\infty = 1$ ($M_0 = \gamma^{1/2}$), and $(u_\infty, v_\infty) = (1, 1)$. An isentropic vortex is added to this mean flow field. The perturbation values are given by

$$(\delta u, \delta v) = \frac{\lambda}{2\pi} e^{\eta(1-s^2)}(-\bar{y}, \bar{x}) \tag{20}$$

$$\delta T = -\frac{(\gamma-1)\lambda^2}{16\eta\gamma\pi^2} e^{2\eta(1-s^2)}, \tag{21}$$

where $(\bar{y}, \bar{x}) = (x - x_0, y - y_0)$, $x_0$ and $y_0$ are the coordinates of the center of the vortex at the initial time (in this study $(x_0, y_0) = (5, 5)$), and $s^2 = \bar{x}^2 + \bar{y}^2$. The entire flow is required to be isentropic, so $p = \rho^\gamma$ with

$$\rho = (T_\infty + \delta T)^{1/(\gamma-1)} = \left[1 - \frac{(\gamma-1)\lambda^2}{16\eta\gamma\pi^2} e^{2\eta(1-s^2)}\right]^{1/(\gamma-1)}. \tag{22}$$

The computational domain is taken as $[0, 10] \times [0, 10]$ and periodicity is imposed in both directions. The vortex strength $\lambda$ is set to 5, and $\eta$ is chosen equal to 1, instead of 0.5 in [14], to increase the gradients of the solution. The solution is computed with $N$ grid points in each direction (with $N = 20$, 40, 80, 160, and 320). The $L_1$ and $L_2$ errors are computed for all grids at $t = 2$ as in [15]. Those errors (and the corresponding order of accuracy) are reported respectively in Tables I and II for the variable $\rho$. The CFL number is set to 0.5 in all cases. It was verified that the errors reported in the aforementioned tables do not depend significantly on the prescribed time step even at the highest resolution. For example, the C4 scheme gives a $L_1$ error equal to 2.39 $10^{-7}$ with $N = 320$ at CFL = 0.05, whereas, at CFL = 0.5, the $L_1$ error is equal to 2.41 $10^{-7}$ (see Table I). The results can be summarized as follows. The C4 and WENO schemes converge toward their expected order of accuracy (respectively 4 and 5) on the finest grid. The ENO scheme gives results close to their formal order of accuracy, whereas the order of accuracy of the MUSCL scheme is slightly larger than 2. Note that the error of the MUSCL scheme doubles with a compression factor of the minmod function set to 1 instead of 4 (as in the presented results). Concerning shock-capturing schemes used as characteristic-based filters, one can notice that the WENO–ACM scheme is fourth-order accurate for the highest resolutions. This demonstrates, on the one hand, that the order of accuracy of the base scheme is not affected if a higher order scheme is used as filter, and,

**TABLE I**

**$L_1$ Error for the Variable $\rho$ at $t$ = 2**

| $N$ | | C4 | ENO | MUSCL | WENO | ENO–ACM | MUSCL–ACM | WENO–ACM |
|---|---|---|---|---|---|---|---|---|
| 20 | $L_1$ error | 1.08E-2 | 7.83E-3 | 9.33E-3 | 6.12E-3 | 5.63E-3 | 6.18E-3 | 4.61E-3 |
| | $L_1$ order | — | — | — | — | — | — | — |
| 40 | $L_1$ error | 1.13E-3 | 1.28E-3 | 2.39E-3 | 9.39E-4 | 7.81E-4 | 1.29E-3 | 6.11E-4 |
| | $L_1$ order | 3.26 | 2.61 | 1.96 | 2.70 | 2.85 | 2.26 | 2.91 |
| 80 | $L_1$ error | 5.78E-5 | 2.08E-4 | 5.99E-4 | 7.07E-5 | 6.68E-5 | 2.81E-4 | 4.58E-4 |
| | $L_1$ order | 4.29 | 2.62 | 1.99 | 3.73 | 3.55 | 2.19 | 3.74 |
| 160 | $L_1$ error | 3.79E-6 | 3.01E-5 | 1.26E-4 | 2.46E-6 | 7.84E-6 | 5.31E-5 | 2.95E-6 |
| | $L_1$ order | 3.93 | 2.79 | 2.25 | 4.84 | 3.09 | 2.40 | 3.97 |
| 320 | $L_1$ error | 2.41E-7 | 4.07E-6 | 2.26E-5 | 8.52E-8 | 6.82E-7 | 8.61E-6 | 2.13E-7 |
| | $L_1$ order | 3.97 | 2.89 | 2.47 | 4.85 | 3.52 | 2.62 | 3.79 |

**TABLE II**
**$L_2$ Error for the Variable $\rho$ at $t = 2$**

| $N$ | | C4 | ENO | MUSCL | WENO | ENO–ACM | MUSCL–ACM | WENO–ACM |
|---|---|---|---|---|---|---|---|---|
| 20 | $L_2$ error | 1.93E-2 | 2.45E-2 | 2.90E-2 | 1.90E-2 | 1.77E-2 | 1.97E-2 | 1.45E-2 |
| | $L_2$ order | — | — | — | — | — | — | — |
| 40 | $L_2$ error | 2.92E-3 | 4.09E-3 | 8.29E-3 | 3.16E-3 | 2.47E-3 | 4.05E-3 | 2.08E-3 |
| | $L_2$ order | 2.72 | 2.58 | 1.81 | 2.59 | 2.84 | 2.28 | 2.80 |
| 80 | $L_2$ error | 1.90E-4 | 6.75E-4 | 2.26E-3 | 2.64E-4 | 2.08E-4 | 1.14E-3 | 1.48E-4 |
| | $L_2$ order | 3.94 | 2.60 | 1.88 | 3.58 | 3.57 | 1.83 | 3.81 |
| 160 | $L_2$ error | 1.23E-5 | 8.69E-5 | 5.91E-4 | 1.10E-5 | 2.51E-5 | 3.12E-4 | 9.44E-6 |
| | $L_2$ order | 3.95 | 2.96 | 1.94 | 4.58 | 3.05 | 1.87 | 3.97 |
| 320 | $L_2$ error | 7.84E-7 | 1.33E-5 | 1.31E-4 | 2.93E-7 | 2.19E-6 | 6.07E-5 | 6.85E-7 |
| | $L_2$ order | 3.97 | 2.71 | 2.17 | 5.23 | 3.52 | 2.36 | 3.78 |

on the other hand, that it is unnecessary to use a filter of higher order than the base scheme. The ENO–ACM gives intermediate results (order of accuracy of about 3.5) between the fourth-order accurate, C4 base scheme and the third-order accurate, ENO scheme. This constitutes evidence that the global order of accuracy is not limited in practice to the lowest order of accuracy between the base scheme and the filter. This statement is unfortunately not general since the MUSCL–ACM scheme gives nearly the same order of accuracy as the MUSCL scheme. However, the values of the error are about two times lower with the MUSCL–ACM scheme than with the MUSCL scheme (with $N = 320$).

To complete the previous results, the evolution of the density along the line $y = 7$ is plotted in Fig. 1. An enlargement is provided near the center of the vortex ($x = 7$). This plot

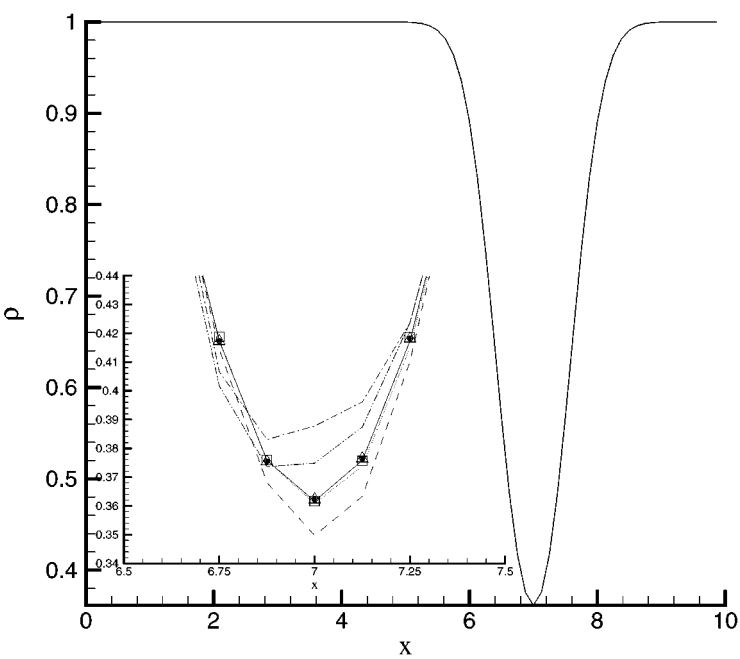


**FIG. 1.** Longitude cut of the density at $y = 7$ ($N = 80$). Ref —, ENO – – –, MUSCL -·-·-·, WENO □, ENO–ACM · · ·, MUSCL–ACM -···-···-, WENO–ACM △, C4 ●.

**TABLE III**
**CPU Time (in Second per Grid Points and per Time Step) and MFlops Obtained for the Tested Schemes (NEC SX5, $N$ = 320)**

| | C4 | ENO | MUSCL | WENO | ENO–ACM | MUSCL–ACM | WENO–ACM |
|---|---|---|---|---|---|---|---|
| CPU times | 9.1E-8 | 1.8E-6 | 5.7E-7 | 1.5E-6 | 7.9E-7 | 3.2E-7 | 7.4E-7 |
| MFlops | 3653 | 1388 | 3440 | 3264 | 1718 | 2900 | 3056 |

confirms the improvement provided by the characteristic-based filters. Note that the ENO and ENO–ACM schemes exhibit a slightly antidissipative behavior which has already been observed in an other study [19]. But, one has to mention that this behavior is observed only with the modification introduced in [18] (bias of the stencil selection). A classical ENO [10] is less precise but always exhibits a dissipative behavior.

The results presented here concerning MUSCL schemes may appear of poor quality compared to those presented in [7]. The case of the advection of an isentropic vortex was also carried out by these authors (density profiles are provided for a large time). But, in this case for which the flow does not contain any discontinuity, the value of $\kappa$ was set to 0.05, a value which does not allow the treatment of cases with shocks. Note that with $\kappa = 0.05$, the MUSCL–ACM scheme gives errors six times lower than with $\kappa = 1$ (for $N = 320$).

Another advantage of using the shock-capturing schemes as filter is the reduction of the computational time. The CPU times, given in second per grid points and per time step, and the computational efficiency, given in MFlops, are reported in Table III for each scheme. Of course, the performance of an algorithm is developer dependent and these values must not be considered as optimal. We just guarantee that the same effort of optimization has been performed for each scheme. These evaluations (for $N = 320$) has been performed with a NEC SX5 vector supercomputer using one processor.

The ratio of the computational time reaches 1.8 between the MUSCL and MUSCL–ACM schemes and about 2.3 between the ENO and WENO schemes and their ACM counterparts. For a very CPU time consuming, shock-capturing scheme this ratio could be as high as the number of substeps in the Runge-Kutta scheme i.e., 3 for the Runge-Kutta scheme used in this study). The MUSCL scheme is three time less expensive than the WENO scheme but, for a computational cost reduced to a factor of 8 ($N = 160$), the error remains 10 times lower for the WENO scheme than for the MUSCL one (with $N = 320$). The same conclusion can be drawn (to a slightly lesser extent) by comparing MUSCL–ACM and WENO–ACM schemes. Despite a lower precision for the ENO scheme than for the WENO scheme, the ratio precision/computational cost is better for the ENO (and ENO–ACM) schemes than for the MUSCL (and MUSCL–ACM) ones. As mentioned by Jiang and Shu [12], the ENO scheme is not cost effective (1388 MFlops) mainly because the choice of the stencil involves heavy usage of logical statements. One can remark that the centered C4 scheme offers the best compromise precision/computational cost but its application is limited to regular solutions of the Navier–Stokes equations.

### 3.2. *Interaction of a Moving Shock with a Density Wave*

This test case (introduced in [10]) allows us to check the capability of characteristic-based filters in the presence of shock. The one-dimensional Euler equations are solved in a

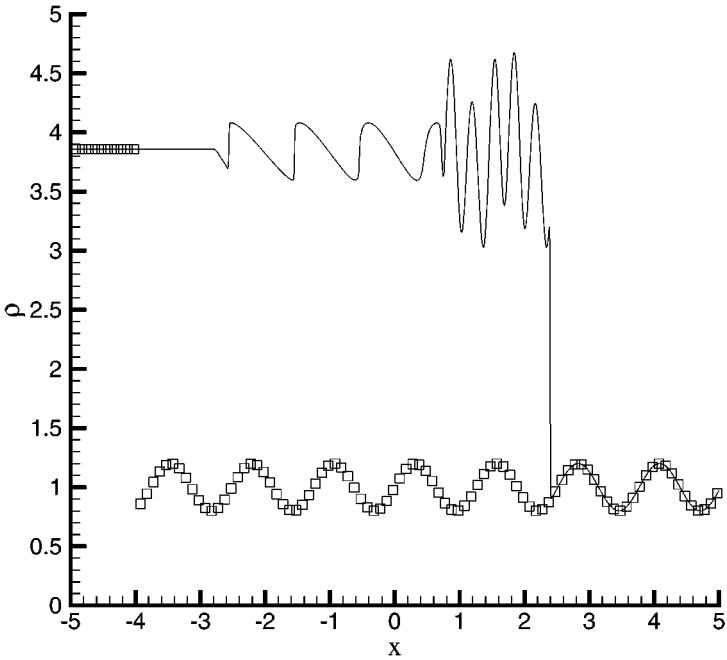


**FIG. 2.** Evolution of the density (full computational domain). Initial time □, final time (reference solution) —.

domain of length $[-5, 5]$. The Mach number is set to 3 and the initial state is defined as

$$\begin{array}{llll} \rho = 3.857143; & u = 2.269369; & P = 10.33333 & \text{for } x < -4 \\ \rho = 1 + 0.2\sin(5x); & u = 0; & P = 1 & \text{for } x \geq -4. \end{array} \tag{23}$$

The solution is advanced in time up to $t = 1.8$. The initial and final solutions on the full computational domain are presented in Fig. 2. A reference solution is computed with a fifth-order accurate, WENO scheme with $N = 1600$ grid points.

This solution, noted REF, is compared with the solution given by the previously used, shock-capturing schemes with $N = 200$ and $N = 400$ grid points. The ENO, MUSCL, and WENO schemes are compared to their counterpart as characteristic-based filters in Figs. 3, 4, and 5 respectively. These figures show the evolution of the density in the range [0, 3], where the solution varies fastly. The global conclusion is that the use of the ACM switch improves the quality of results for all schemes on both grids. As already mentioned in [10], we observe that ENO schemes behave better than MUSCL schemes for this test case whatever the resolution. The use of MUSCL scheme as filter does not allow this scheme to recover a precision comparable to the ENO schemes (deprived of the ACM switch). For $N = 400$, the improvement involved by the ACM switch is less sensible for the WENO scheme, which is already very precise, than for the classical ENO scheme. For $N = 200$, the WENO–ACM scheme is closer to the reference than the ENO–ACM scheme (in particular near $x = 1.2$), whereas, for $N = 400$, the ENO–ACM scheme exhibits better results than the WENO–ACM scheme. This may be due to the slightly antidissipative behavior of the ENO scheme already mentioned in the discussion concerning the previous test case (see in particular near $x = 1.7$, where the ENO scheme exceeds the reference solution).

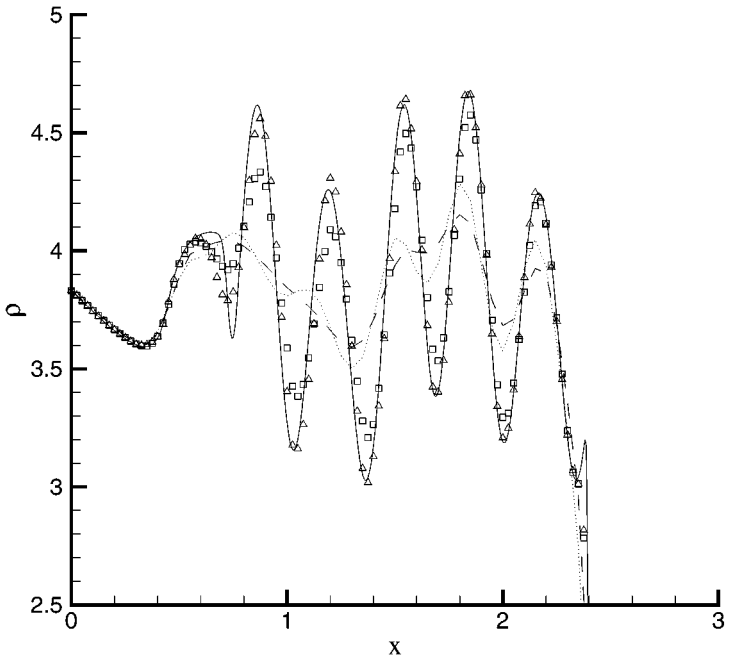


**FIG. 3.** Evolution of the density. Ref —, ENO ($N = 200$) − − −, ENO–ACM ($N = 200$) $\cdots$, ENO ($N = 400$) $\square$, ENO–ACM ($N = 400$) $\triangle$.

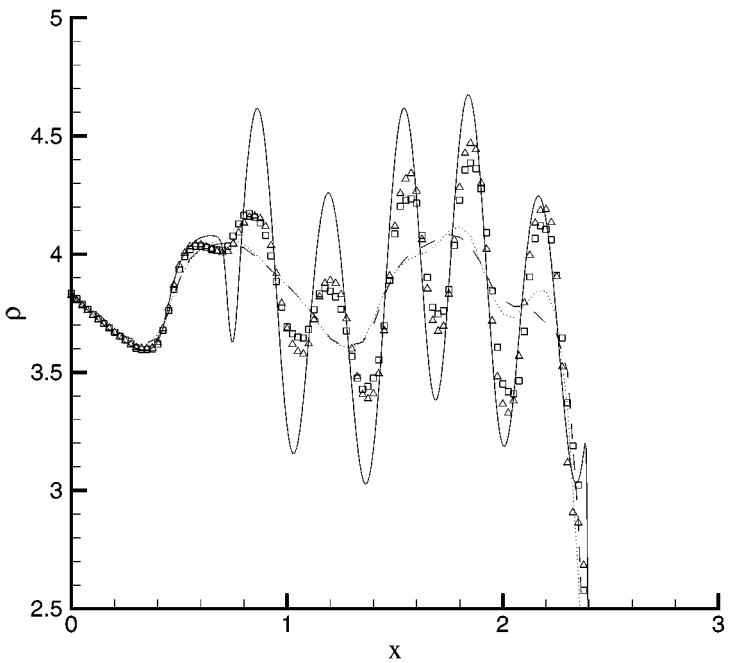


**FIG. 4.** Evolution of the density. Ref —, MUSCL ($N = 200$) − − −, MUSCL–ACM ($N = 200$) $\cdots$, MUSCL ($N = 400$) $\square$, MUSCL–ACM ($N = 400$) $\triangle$.

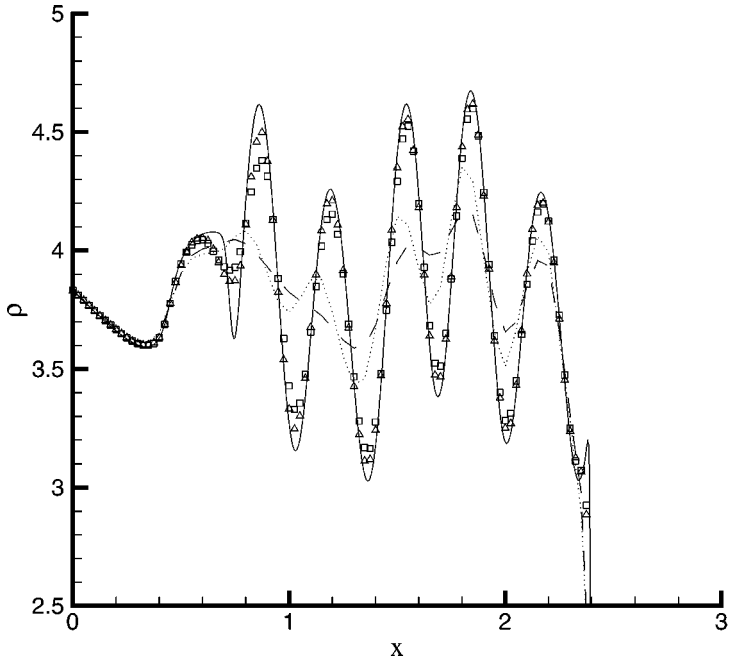


**FIG. 5.** Evolution of the density. Ref —, WENO ($N = 200$) – – –, WENO–ACM ($N = 400$) $\cdots$, WENO ($N = 400$) $\square$, WENO–ACM ($N = 400$) $\triangle$.

The results presented here clearly demonstrate the necessity of the use of the better possible shock-capturing scheme even when the effects of the numerical dissipation are minimized by means of the ACM switch.

### 3.3. *Shock-Vortex Interaction*

This test case was originally designed to investigate the capability of the shock-capturing schemes to predict the generation and the transport of acoustic waves during a shock/vortex interaction. Comparisons of different types of TVD and ENO schemes are presented in [16] using this test case, and ENO schemes were shown to transport acoustic fluctuations better than TVD schemes.

A squared computational domain $2L_0 \times 2L_0$ is considered. A stationary plane weak shock is located at $x_0 = 1$; the Mach number is 1.1588. The uniform flow is initialized using the Rankine–Hugoniot relationships. The Reynolds number based on the characteristic of the uniform flow and the length $L_0$ is equal to $\mathrm{Re} = 2000$. A Taylor vortex defined as

$$V_\theta(r) = C_1 r \cdot e^{-C_2 r^2}, \tag{24}$$

with

$$C_1 = \frac{U_c}{r_c}\, e^{1/2}; \quad C_2 = \frac{1}{2r_c^2}; \quad r = ((x - x_0)^2 + (y - y_0)^2)^{1/2},$$

is superimposed on the base flow. The initial position of the vortex center is $x_0 = 1/2$, $y_0 = 1$. The presented results have been obtained with a radius $r_c = 0.075$ and a maximum dimensionless velocity $U_c = 0.25$. Following these values, the viscous core radius is $1/2$.

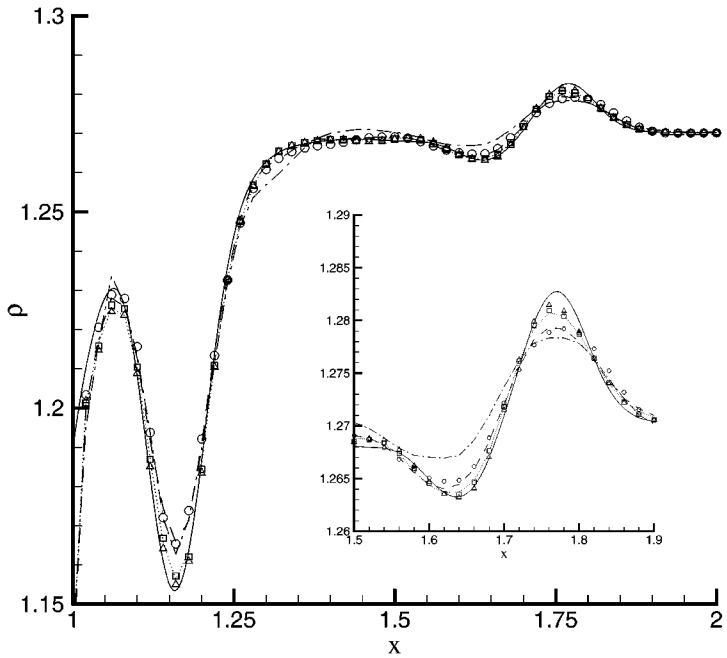


**FIG. 6.** Longitude cut of the density at $y = 1$ and $t = 0.7$. C6 —, ENO – – –, MUSCL -·-·-·, WENO □, ENO–ACM · · ·, MUSCL–ACM ◯, WENO–ACM △.

At the inflow boundary, the supersonic mean flow allows us to prescribe all the conservative variables. On the outflow boundary, a nonreflecting boundary condition is applied. Computations are performed with 101 uniformly distributed grid points in both directions. A reference solution have been computed [6] with a sixth-order accurate, compact scheme [20] (noted C6) on a very fine uniform grid including $801 \times 501$ grid points. The calculations have been performed using a CFL number equal to 0.5 up to a dimensionless time equal to 0.7.

Figure 6 represents the longitudinal evolution of the density on a line $y = 1$ and $t = 0.7$ in the post-shock zone ($1 \leq x \leq 2$). The vortex center is located at $x = 1.16$ and the perturbation induced by the propagating acoustic waves is visible around $x = 1.75$. The improvement of the solution is very clear between the ENO scheme and the ENO–ACM scheme both for the deficit of density in the vortex core and for the acoustic wave. Between the MUSCL and MUSCL–ACM schemes, the improvement is less sensible than for the ENO schemes both for the vortex and for the acoustic waves. Nevertheless, in the intermediate zone (between $x = 1.25$ and $x = 1.6$), one can observe that the spurious behavior of the MUSCL scheme is corrected by the ACM switch. This strange behavior may be related to the overcompressive feature of this scheme (with a minmod limiter used with a compression factor set equal to 4). Such kind of problem has been previously observed with this scheme in [16]. The WENO scheme gives very accurate results which are only slightly improved by the adjunction of the ACM switch. We recall that the global order of accuracy of the WENO scheme (fifth-order of accuracy) is larger than that of the WENO–ACM scheme (fourth-order of accuracy).

This first set of numerical tests demonstrates clearly the improvement provided by the characteristic based filters whatever the filters used (ENO, WENO, or MUSCL). The ENO

filters are seen to give more accurate results than the TVD–MUSCL filters. However, the behavior of this approach on a fully turbulent case must be investigated.

## 4. ASSESSMENT OF DISCONTINUITY SENSORS

The use of the sensor introduced by Ducros *et al.* [9] is particularly interesting in the framework of the simulation of a fully turbulent flow (DNS or LES). Two turbulent test cases are now considered to evaluate Ducros *et al.* [9] and ACM sensors: freely decaying homogeneous turbulence and shock/homogeneous turbulence interaction. In the first case, our goal is to prove the capacity of the presented approach in a wide range of initial conditions previously documented in DNS by Cai *et al.* [21]. The second test case was treated by Lee *et al.* [2, 22] using DNS and later, with the same parameters, by Ducros *et al.* [9] using LES and by Garnier *et al.* [3, 4] using DNS and LES. In [2–4], the information concerning the mean position of the shock is used to apply the shock-capturing scheme only on a few grid points around this mean position. Here, the objective is to assess the behavior of each sensor in a case for which the sensors are supposed to concentrate the numerical dissipation locally. The evaluation is limited to ENO filters because these two test cases have been initially studied with ENO scheme (see [21] and [22]). In this study, the effect of the sensors is investigated by comparing ENO scheme (applied locally in the second turbulent test case), ENO–ACM scheme, $\Psi$-ENO–ACM scheme, and $\Psi$-ENO scheme. Although the goal of this study is not to demonstrate any improvement over the approach presented in [9], both test cases have also been treated with the $\Psi$-Jameson scheme (which has been used in [9] to compute the shock/turbulence interaction test case). This gives a useful reference.

### 4.1. *Compressible Freely Decaying Homogeneous Turbulence*

*4.1.1. Description of the test case.* Compressible homogeneous turbulence is known to depend mostly on two parameters: turbulent Mach number $M_t$ and compressibility factor $\chi$. The turbulent Mach number is defined as $M_t = q/\overline{c}$ (where $q = \langle u_i' u_i' \rangle^{1/2}$ and $\overline{c} = (\gamma R T_0)^{1/2}$). Assuming an Helmholtz decomposition of the velocity field, the compressibility factor is defined as the ratio between compressible fluctuating kinetic energy and total (compressible plus solenoidal) fluctuating kinetic energy. In [21], the objective is to investigate the effect of these two parameters on turbulence initially dominated by fluctuations of temperature. In this study, we use the same framework to investigate the effect of the compressibility factor on the tested scheme. Indeed, with $\chi = 1$, the robustness of schemes based on the filtering is to be demonstrated. With medium ($\chi = 0.6$) and zero values of the compressibility ratio, the influence of sensors is supposed to be of relatively less importance in DNS where the numerical dissipation introduced by numerical schemes is expected to be weak.

The parameters of the computations are reported in Table IV. The other physical parameters and the initial turbulent spectrum are the same as in Cai *et al.* [21] and the fluctuations of

**TABLE IV**
**Initial Values of $M_t$ and $\chi$ for the Three Test Cases**

| | Case S | Case R | Case L |
|---|---|---|---|
| $M_t$ | 0.3 | 0.3 | 0.3 |
| $\chi$ | 0 | 0.6 | 1 |

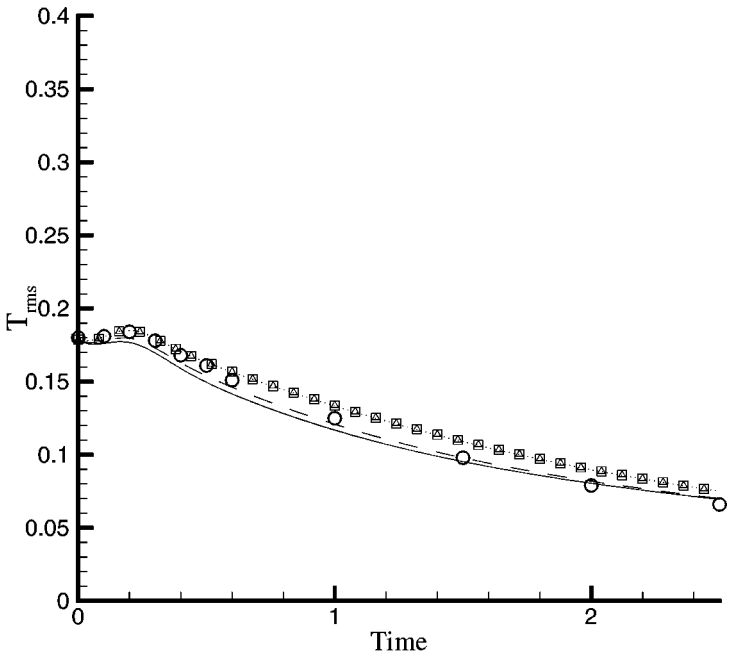


**FIG. 7.** Time evolution of the fluctuating temperature (case S). REF ◯, ENO —, ENO–ACM – – –, Ψ-ENO–ACM □, Ψ-ENO · · · , Ψ-Jameson △.

thermodynamic quantities are initialized with the procedure described in [21] . The boundary conditions are periodic in the three directions. As in [21], the time is nondimensionalized by the initial eddy, turnover time.

*4.1.2. Results.* The fluctuating temperature obtained with ENO, ENO–ACM, Ψ-ENO–ACM, Ψ-ENO, and Ψ-Jameson schemes are displayed with the results obtained in [21] (denoted REF) in Figs. 7–9 for the test cases S, R and L respectively. The general agreement between REF and the tested schemes is good considering some small imprecisions in the definition of the ENO scheme used in [21]. The proposed approach does not suffer from numerical stability problems in particular in the very demanding case L. For the newly introduced scheme, a value of the fluctuating temperature larger than the one of the classical ENO scheme is interpreted as evidence of a lower value of the introduced numerical dissipation. Note that the evolution of the fluctuating kinetic energy (not shown) is highly correlated with the evolution of the fluctuating temperature and that, in the frame of decaying homogeneous turbulence, a lower value of the kinetic energy is often interpreted as the consequence of a lower numerical dissipation.

Following this interpretation, the dissipation is seen to be reduced by both sensors in cases S and R for all schemes and in case L for schemes based on ENO filters. In the latter case, the dissipation introduced by the Ψ-Jameson appears to be larger than the one introduced by the Ψ-ENO scheme while the results of these two schemes based on the Ψ sensor are very close in the two other cases.

From the results presented in Figs. 7–9, it is not possible to draw clear-cut conclusions about the relative importance of the dissipation introduced by each sensor. This issue will be addressed in the shock/homogeneous turbulence test case.

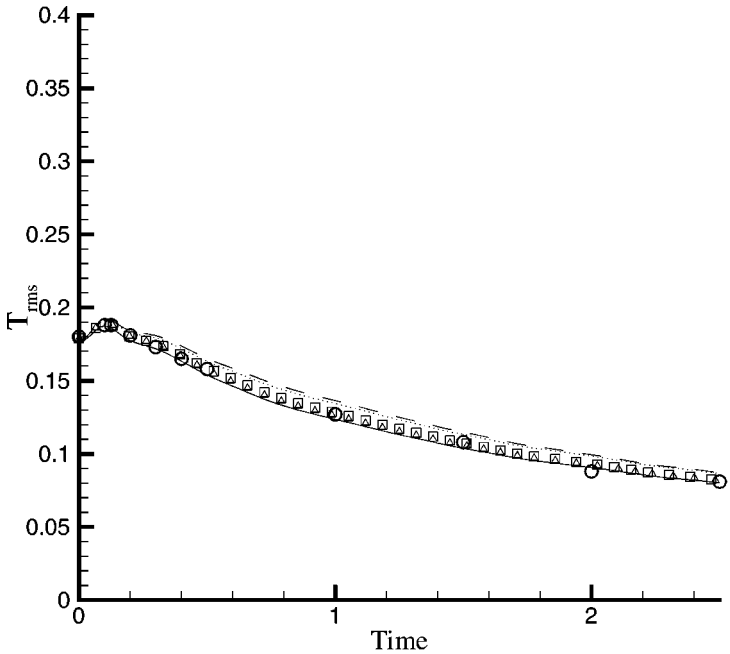


**FIG. 8.** Time evolution of the fluctuating temperature (case R). REF ◯, ENO —, ENO–ACM – – –, Ψ-ENO–ACM □, Ψ-ENO · · · , Ψ-Jameson △.

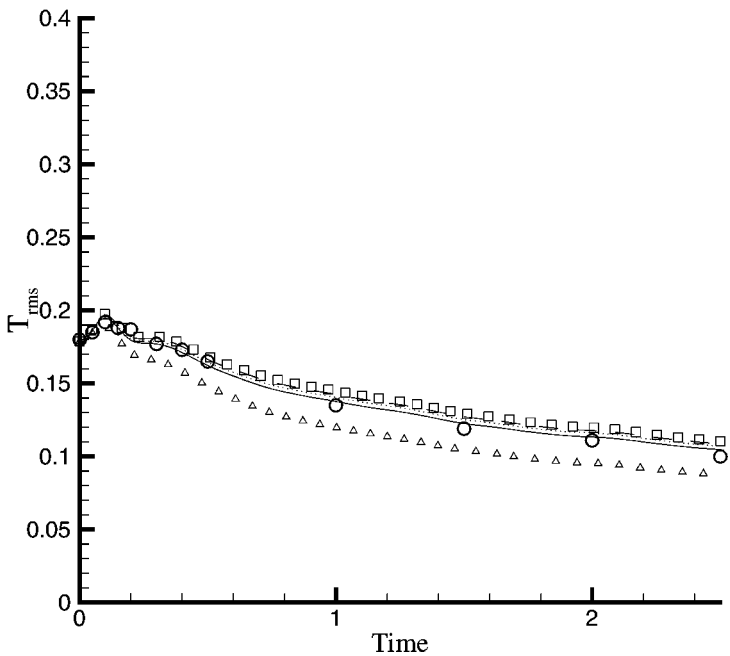


**FIG. 9.** Time evolution of the fluctuating temperature (case L). REF ◯, ENO —, ENO–ACM – – –, Ψ-ENO–ACM □, Ψ-ENO · · · , Ψ-Jameson △.

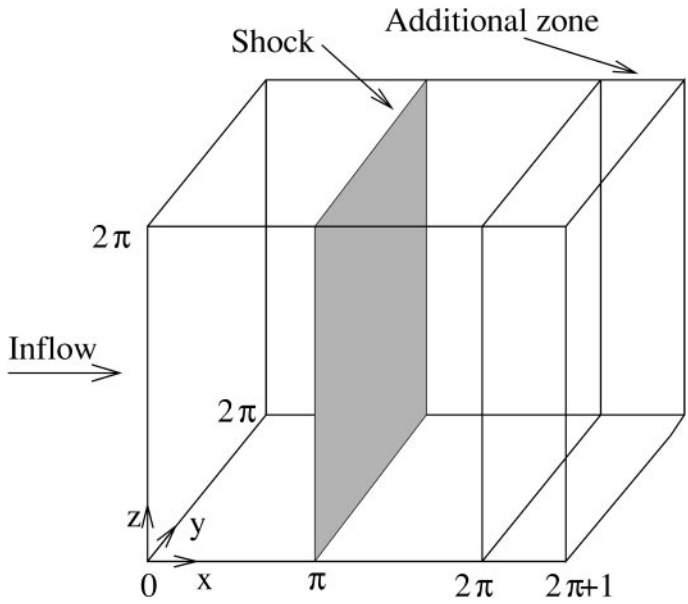


**FIG. 10.** Description of the configuration.

4.2. *Shock/Homogeneous Turbulence Interaction*

*4.2.1. Description of the configuration.* The simulations are performed in a coordinate system fixed with respect to the mean shock position where the flow is supersonic upstream and subsonic downstream. The direction of the mean flow is chosen to be normal to the shock wave, aligned with the $x$ axis (see Fig. 10).

Simulations are performed in a cubic box of length $2\pi$ which is completed by a zone of length 1 with a highly stretched mesh. This zone, combined with Thompson outflow conditions [23], provides satisfactory nonreflecting behavior. The position of the shock is prescribed at $x = \pi$. At the inflow, a realistic turbulent field obtained by means of a simulation of freely decaying turbulence is introduced via Taylor's hypothesis. At the initial time, a uniform flow satisfying the Rankine–Hugoniot jump relations is imposed and the turbulent fluctuations are introduced at the inflow. Statistics are collected by averaging in time and the homogeneous directions $y$ and $z$. Brackets $\langle\ \rangle$ denote this ensemble average operator. The fluctuation variance of a variable $\zeta$ is noted $\langle\zeta'^2\rangle = \langle\zeta^2\rangle - \langle\zeta\rangle^2$ and $\zeta_{\text{rms}} = (\langle\zeta'^2\rangle)^{1/2}$.

The Mach number is set equal to 1.2. The turbulent Mach number is equal to 0.136. The Reynolds number based on the longitudinal Taylor microscale $\lambda$ : $\text{Re}_\lambda = \rho u_{\text{rms}}\lambda/\mu$ is equal to 11.9 and the peak wave number $k_0$ of the inflow spectrum (of shape $\sim (k/k_0)^4\exp(-2k^2/k_0^2)$) is taken equal to 6 ($k_0$ fixes the inflow Taylor microscale ($k_0\lambda = 2$)). The parameters $M_t$ and $\text{Re}_\lambda$ are taken at the location immediately upstream of the shock.

The number of grid points in the shock-normal direction is 69 and the SGS model is the Smagorinsky model (see [4] for further details concerning both the influence of the resolution in the shock-normal direction and the influence of the SGS model).

In the homogeneous directions ($y$ and $z$), periodicity is imposed and 32 grid points are uniformly distributed ($\Delta y = \Delta z$), a fourth-order accurate, centered skew-symmetric

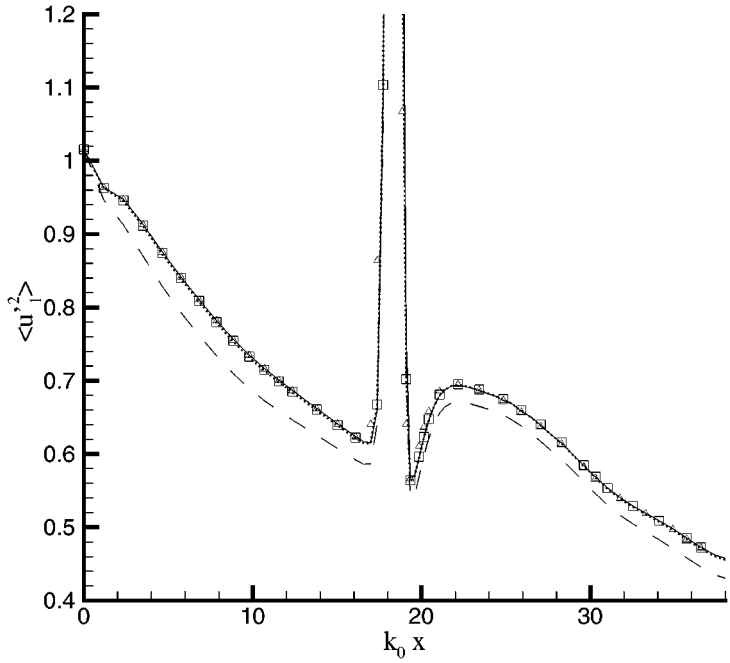


**FIG. 11.** Evolution of the streamwise velocity variance. LENO —, ENO–ACM – – –, Ψ-ENO–ACM □, Ψ-ENO · · ·, Ψ-Jameson △.

scheme is used for the convective flux. This technique of discretization is known to reduce the aliasing errors [24]. In this study, the approach (referred to as LENO for Local ENO), developed in [2–4] in which the ENO scheme is applied to a zone of length arbitrarily fixed, is compared to the ENO–ACM, Ψ-ENO–ACM, Ψ-ENO, and Ψ-Jameson approaches.

*4.2.2. Results.* The evolution of the streamwise (resp. transverse) velocity variance is given in Fig. 11 (resp. Fig. 12) The amplification of the turbulence downstream of the shock ($k_0x > 21$) is reproduced by all schemes. As explained in [22], the shock oscillations due to the streamwise component of turbulence intensity lead to a local overprediction of the turbulence statistics near the shock. The evolution of the statistics in this zone (near $k_0x = 18$) is not to be discussed. Ψ-ENO–ACM, Ψ-ENO, and Ψ-Jameson schemes give results very close to the LENO scheme for both component of the velocity. This suggests that the sensor of Ducros *et al.* [9] ensures an application of the dissipation as local as with the fixed zone of the LENO scheme. In contrast, the ENO–ACM scheme exhibits an overdissipative behavior. This shows that the ACM switch is not able to distinguish between a turbulent fluctuation and a shock. The ENO filter is then applied to a significative proportion of the grid points. The results of the Ψ-ENO and Ψ-Jameson schemes are so close that one can conclude that in this particular test case the values of the dissipation introduced by these schemes are quasi-identical.

In order to verify those assumptions concerning the effect of both sensors, the mean values of the sensor Ψ and $\Psi \times \theta^1$ (which multiplies the ENO dissipation) for the Ψ-ENO–ACM scheme are compared to the mean values of the ACM switch for the ENO–ACM scheme and to the mean values of the Ψ sensor for the Ψ-ENO and the Ψ-Jameson scheme (Fig. 13).

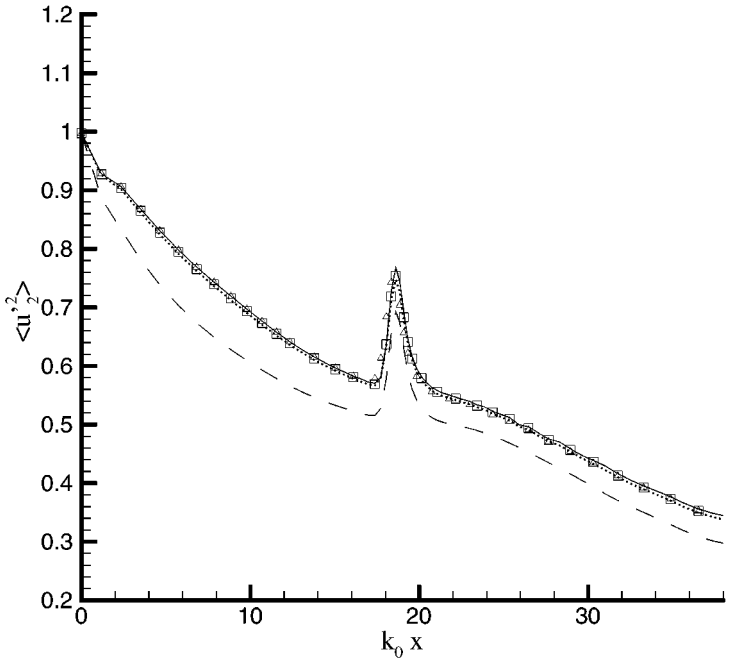


**FIG. 12.** Evolution of the transverse velosity variance. LENO —, ENO–ACM – – –, Ψ-ENO–ACM □, Ψ-ENO · · · , Ψ-Jameson △.

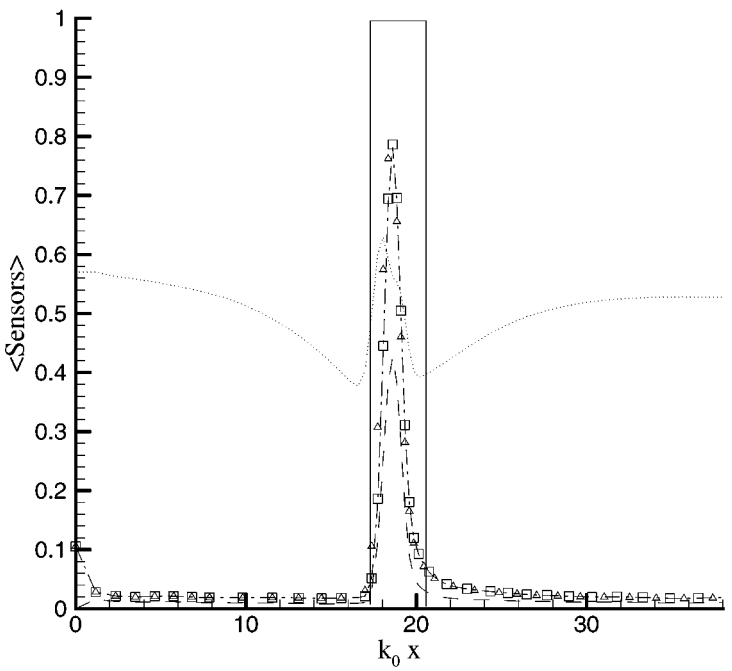


**FIG. 13.** Streamwise evolution of the sensors: LENO —, $\theta^1 \times \Psi$ for Ψ-ENO–ACM – – –, Ψ for Ψ-ENO–ACM -·-·-, $\theta^1$ for ENO–ACM · · · , Ψ-ENO □, Ψ-Jameson △.

We recall that $\theta^1$ is the ACM switch associated with the eigenvalue $a^1$ (namely $u$). It was verified that the behavior of $\theta^l$ for $l \neq 1$ does not exhibit significant difference with $\theta^1$. The ACM sensor varies smoothly and its value remains close to 0.6, whereas, for all schemes, the Ducros *et al.* [9] sensor takes a value close to 0.8 in the shock zone and less than 0.05 elsewhere. Consequently, the dissipation of the ENO–ACM scheme is applied everywhere with nearly the same intensity. This explains the overdissipative behavior of this scheme observed in Figs. 11 and 12. In contrast, the use of the Ducros *et al.* [9] sensor allows the application of the numerical dissipation quasi-exclusively in the shock zone. Note that the size of the ENO zone for the LENO scheme is also reported in Fig. 13.

## 5. CONCLUSION

Explicit ENO and WENO filters have been developed and compared with classical ENO schemes, TVD filters, and classical TVD schemes. First, the precision of the aforementioned schemes was investigated on three test cases: the advection of an isentropic vortex, the interaction of a density wave with a shock, and the shock/vortex interaction. The general conclusion is that the ACM switch improves the quality of results with respect to the classical approach, whatever the shock-capturing scheme used as filter. Moreover, the ACM switch gives better results when it is associated with the ENO schemes than when associated with the MUSCL scheme. From a practical point of view, it is demonstrated that it is unnecessary to use a filter of higher order accuracy than the base scheme. Furthermore, the ACM switch corrects the spurious behavior of the MUSCL scheme observed in the propagation of an acoustic wave. In a second part, we have compared the ACM and Ducros *et al.* [9] sensors. The general conclusion is that the ACM sensor is not able to distinguish a turbulent fluctuation from a shock, whereas this goal is easily reached for the Ducros *et al.* [9] sensor. For applications involving turbulent flows, the use of this sensor is highly recommended. This allows the control of numerical dissipation in LES of flows including shocks. The coupling of the two sensors ($\Psi$-ACM–ENO scheme) can also be considered for future work.

## REFERENCES

1. E. Garnier, M. Mossi, P. Sagaut, P. Comte, and M. Deville, On the use of shock-capturing scheme for large-eddy simulation, *J. Comput. Phys.* **153**, 273 (1999).
2. S. Lee, S. K. Lele, and P. Moin, Interaction of isotropic turbulence with shock waves: Effect of shock strength, *J. Fluid Mech.* **340**, 225 (1997).
3. E. Garnier, P. Sagaut, and M. Deville, Large-eddy simulation of shock/homogeneous turbulence interaction, *Comput. Fluids*, in press.
4. E. Garnier, P. Sagaut, and M. Deville, Large-eddy simulation of shock/homogeneous turbulence interaction, in *Direct and Large-Eddy Simulation III*, edited by Voke, Sandham, and Kleiser (Kluwer Academic, Dordrecht/Norwell, MA, 1999), p. 123.
5. J. von Neumann and R. D. Richtmyer, A method for the numerical calculation of hydrodynamic shocks, *J. Appl. Phys.* **21**, 232 (1950).
6. B. Engquist, P. Lötstedt, and B. Sjögreen, Nonlinear filters for efficient shock computation, *Math. Comput.* **52**, 509 (1989).
7. H. C. Yee, N. D. Sandham, and M. J. Djomehri, Low-dissipative high-order shock-capturing methods using characteristic-based filters, *J. Comput. Phys.* **150**, 199 (1999).

8. A. Harten, The artificial compression method for computation of shocks and contact discontinuities. III. Self-adjusting hybrid schemes, *Math. Comput.* **32**, 363 (1978).
9. F. Ducros, V. Ferrand, F. Nicoud, C. Weber, D. Darracq, C. Gacherieu, and T. Poinsot, Large-eddy simulation of shock/turbulence interaction, *J. Comput. Phys.* **152**, 517 (1999).
10. C. W. Shu and S. Osher, Efficient implementation of essentially non-oscillatory shock-capturing schemes II, *J. Comput. Phys.* **83**, 32 (1989).
11. H. C. Yee, *A Class of High-Resolution Explicit and Implicit Shock-Capturing Methods*, NASA Technical Memorandum 101088 (1989).
12. G-S. Jiang and C.-W. Shu, Efficient implementation of weighted ENO schemes, *J. Comput. Phys.* **126**, 202 (1996).
13. A. Jameson, W. Schmidt, and E. Turkel, Numerical simulation of the Euler equations by finite volume methods using Runge-Kutta time stepping schemes, AIAA Paper 81-1259, in *AIAA 5th Computations Fluid Dynamics Conference* (1981).
14. C. W. Shu, *Essentially Non-Oscillatory and Weighted Essentially Non-Oscillatory Schemes for Hyperbolic Conservation Laws*, ICASE Report No 97-65 (1997).
15. C. W. Shu, *Weighted Essentially Non-Oscillatory Schemes on Triangular Meshes*, ICASE Report No 98-32 (1998).
16. C. Tenaud, E. Garnier, and P. Sagaut, Evaluation of some high-order shock-capturing schemes for DNS, 2D free flows, *Int. J. Numer. Methods Fluids* **33**, 249 (2000).
17. F. Ducros, F. Laporte, T. Soulères, V. Guinot, P. Moinat, and B. Caruelle, High-order fluxes for conservative skew-symmetric-like schemes in structured meshes: Application to compressible flows, *J. Comput. Phys.* **161**, 114 (2000).
18. C. W. Shu, Numerical experiments on the accuracy of ENO and Modified ENO schemes, *J. Sci. Comput.* **5**, 127 (1990).
19. E. Garnier, P. Sagaut, and P. Comte, ENO and PPM schemes for direct numerical simulation of compressible flows, in *Advances in DNS/LES*, edited by C. Liu, Z. Liu (Greyden, New York, 1997), p. 459.
20. S. K. Lele, Compact finite difference schemes with spectral-like resolution, *J. Comput. Phys.* **103**, 16 (1992).
21. X. D. Cai, E. E. O'Brien, and F. Ladeinde, Thermodynamic behavior in decaying, compressible turbulence with initially dominant temperature fluctuations, *Phys. Fluids* **9**, 1754 (1997).
22. S. Lee, S. K. Lele, and P. Moin, Direct numerical simulation of isotropic turbulence interacting with a weak shock wave, *J. Fluid Mech.* **251**, 533 (1993).
23. K. W. Thompson, Time dependent boundary conditions for hyperbolic system, *J. Comput. Phys.* **68**, 1 (1987).
24. G. A. Blaisdell, E. T. Spylopoulos, and J. H. Qin, The effect of the formulation of nonlinear terms on aliasing errors in spectral methods, *Appl. Numer. Math.* **21**, 207 (1996).